View metadata, citation and similar papers at core.ac.uk

brought to you by CORE

provided by KITopen

New Journal of Physics
The open access journal at the forefront of physics

Deutsche Physikalische Gesellschaft DPG IOP Institute of Physics

PAPER • OPEN ACCESS

Thermal conductivity of isotopically controlled silicon nanostructures

To cite this article: H Bracht *et al* 2014 *New J. Phys.* **16** 015021

View the article online for updates and enhancements.

Related content

- Nanoscale thermal transport in self-organized epitaxial Ge nanostructures on Si(001)
T Frigge, B Hafke, V Tinnemann et al.

- Thermal conductivity of silicene nanosheets and the effect of isotopic doping
Bo Liu, C D Reddy, Jinwu Jiang et al.

- One dimensional Si/Ge nanowires and their heterostructures for multifunctional applications—a review
Samit K Ray, Ajit K Katiyar and Arup K Raychaudhuri

Recent citations

- Effects of heterogeneity and prestress field on phonon properties of semiconductor nanofilms
Jiachuan Wang *et al*

- Atom probe microscopy of zinc isotopic enrichment in ZnO nanorods
C. N. Ironside *et al*

This content was downloaded from IP address 129.13.72.197 on 21/03/2018 at 10:09

New Journal of Physics
The open access journal at the forefront of physics
Deutsche Physikalische Gesellschaft DPG | IOP Institute of Physics

Thermal conductivity of isotopically controlled silicon nanostructures

H Bracht[1,6], S Eon[1], R Frieling[1], A Plech[2], D Issenmann[2], D Wolf[3], J Lundsgaard Hansen[4], A Nylandsted Larsen[4], J W Ager III[5] and E E Haller[5]

[1] Institute of Materials Physics, University of Muenster, Wilhelm-Klemm-Straße 10, D-48149 Muenster, Germany
[2] Institute for Photon Science and Synchrotron Radiation/ANKA, Karlsruher Institute of Technology, Hermann-von-Helmholtz-Platz 1, D-76344 Eggenstein-Leopoldshafen, Germany
[3] University Duisburg-Essen, Faculty of Physics, Lotharstrasse 1, D-47048 Duisburg, Germany
[4] Department of Physics and Astronomy, Ny Munkegade 120, University of Aarhus, DK-8000 Aarhus, Denmark
[5] Lawrence Berkeley National Laboratory, 1 Cyclotron Road, Berkeley, CA 94720, USA
E-mail: bracht@uni-muenster.de

Received 14 August 2013, revised 13 December 2013
Accepted for publication 17 December 2013
Published 17 January 2014
New Journal of Physics **16** (2014) 015021
doi:10.1088/1367-2630/16/1/015021

Abstract
Nanostructured semiconductors open the opportunity to independently tailor electric and thermal conductivity by manipulation of the phonon transport. Nanostructuring of materials is a highly promising strategy for engineering thermoelectric devices with improved efficiency. The concept of reducing the thermal conductivity without degrading the electrical conductivity is most ideally realized by controlled isotope doping. This work reports on experimental and theoretical investigations on the thermal conductivity of isotopically modulated silicon nanostructures. State-of-the-art pump-and-probe experiments are conducted to determine the thermal conductivity of the different nanostructures of isotopically enriched silicon layers epitaxially grown on natural silicon substrates. Concomitant molecular dynamics calculations are performed to study the impact of the silicon isotope mass, isotope interfaces, and of the isotope layer ordering and thickness on the thermal conductivity. Engineering the isotope distribution is a striking concept to reduce the thermal

[6] Author to whom any correspondence should be addressed.

Content from this work may be used under the terms of the Creative Commons Attribution 3.0 licence. Any further distribution of this work must maintain attribution to the author(s) and the title of the work, journal citation and DOI.

1367-2630/14/015021+18$33.00
© 2014 IOP Publishing Ltd and Deutsche Physikalische Gesellschaft

conductivity of silicon without affecting its electronic properties. This approach, using isotopically engineered silicon, might pave the way for future commercial thermoelectric devices.

1. Introduction

The efficient conversion of energy in different energy forms is the grand challenge of the 21st century. Up to now our energy needs are still mainly covered by fossil resources, i.e. solar energy that has been stored during hundreds of millions of years, and by nuclear plants that use the energy stored in heavy uranium isotopes during their formation in e.g. supernova explosions. However, these resources are not only limited but also bear some serious risks as more and more carbon dioxide ends up in the atmosphere and nuclear waste, with long lifetimes, is produced. Sooner or later our energy requirements must be covered by energy plants operating in a sustainable manner. Some progress has been achieved over the past decades in solar energy, wind energy, and waste-to-energy plants that all describe an energy conversion system, that converts sunlight, wind, and the chemical energy of waste e.g. electric energy. Conversion to electricity is highly desirable as the energy can be easily distributed over short and long distances to the consumer, who again converts the electrical energy to e.g. mechanical or chemical energy. The conversion efficiency of fuel gas with the advantage of high energy density (chemical energy) to mechanical energy (potential and kinetic energy) is limited due to thermodynamic principles. These energy conversion systems produce waste heat that limits the efficiency of the process. Considering a general efficiency of 50–70% of today's mechanical heat engines, 50– 30% of energy is lost as waste heat. Often waste heat from industry is used as long-distance heating for public and domestic use but waste heat incurred on the smaller scale is, in general, not used. This for example concerns the heat produced by car engines, lamps and even by the human body. Scalable systems would allow to regain energy in such places. Possibly small autonomous devices could profit, where a supply of external energy is not possible in a sustainable manner. These could, for instance, be remote sensors or miniaturized devices with a need of process-compatible technologies, such as semiconductor thin-film growth [1, 2].

Systems that directly convert heat to electricity are thermoelectric generators. As a solid state device these generators have no moving parts and thus are quite robust and long-lasting. However, the efficiency of such energy conversion systems is very low compared with steam turbines. Moreover, commercial thermoelectric devices are made of bismuth and tellurium. Both the elements are considered as critical raw materials due to their limited availability. In order to promote thermoelectric devices for applications serving our daily life that implies their large-scale production, devices should be fabricated from abundant raw materials and should have an acceptable energy conversion efficiency [3].

Today electronic devices based on silicon (Si) are produced in mass production with high throughput, reliability and performance, thanks to the progress achieved over the past decades in the processing of Si-based nanoelectronic devices. In small autonomous devices, such as remote sensors a high degree of integration and miniaturization is required, which favors process-related materials. Unfortunately, Si, which is one of the most abundant elements of the earth's crust, is not well suited as thermoelectric material as its thermal conductivity is with $150\,\mathrm{W\,m^{-1}K^{-1}}$ too high. The addition of the heavier element germanium (Ge) with up to 50% reduces the

thermal conductivity by a factor of 10 [4]. This reduction is caused by alloy disorder scattering of the phonons due to the high mass difference between Si and Ge host atoms and their random distribution. With increasing Ge content also the electrical conductivity of the SiGe alloys decreases but less strongly than the thermal conductivity. These properties of SiGe alloys result in good figures of merit for thermoelectric applications at high temperatures. However, Ge tends to leave the material at high temperature due to its higher vapor pressure compared to Si. This favors a decomposition of the alloy although it is, in principle, completely miscible. Moreover dopant accumulation degrades the performance of SiGe-based thermoelectric devices.

Similar to the disorder scattering of phonons in SiGe alloys, the thermal conductivity of natural silicon is disturbed by the isotope defects that describe variants of the same chemical element with different atomic mass due to different numbers of neutrons in the nucleus. Natural Si consists of an alloy of the three stable isotopes ^{28}Si(92.2%), ^{29}Si(4.7%) and ^{30}Si(3.1%), where the number in bracket describes the isotopic abundance. In high isotopically enriched material the scattering of phonons at isotope defects is reduced and accordingly ^{28}Si possesses a slightly higher thermal conductivity than natural Si [5–7]. Since the electronic properties of Si, i.e. the band structure, carrier mobility and electronic defect states only weakly depend on the isotope mass [8–10], the thermal conductivity of Si due to phonon transport can be altered specifically by isotope defects without affecting the electronic properties. On the other hand the Seebeck coefficient is not expected to change significantly with isotopic composition for temperatures above room temperature because the electronic contribution to the Seebeck coefficient exceeds the phonon contribution [11, 12].

In this work, the impact of controlled isotope doping on the thermal conductivity of Si is investigated experimentally and theoretically. Various isotopically modulated Si layers are studied including a high-purity ^{28}Si layer and alternating layers of ^{28}Si and ^{29}Si or ^{30}Si. The thermal conductivity of the layers is determined by means of time-resolved x-ray scattering (TRXS). Molecular dynamics calculations are performed to examine the impact of isotope doping, layer ordering and thickness on the thermal conductivity. It is evident that the properly designed isotopically modulated Si nanostructures can exhibit thermal conductivities well below those of isotopically pure and natural Si.

2. Experimental

2.1. Sample preparation

Silicon samples with different isotopically modulated layers were epitaxially grown by means of molecular beam epitaxy (MBE) and chemical vapor deposition (CVD) on (100) oriented Si wafers of natural isotopic abundance. Twenty undoped bilayer structures of $(^{29}\mathrm{Si}/^{28}\mathrm{Si})_{20}$ (sample #1) and $(^{30}\mathrm{Si}/^{28}\mathrm{Si})_{20}$ (sample #2) were grown by MBE on p-type substrates (boron doped) with a specific resistivity of ~ 0.02 and $\sim 4\,\Omega\,\mathrm{cm}$, respectively. The thickness of each individual isotope layer is about 10 nm resulting in a total thickness of about 400 nm for the entire layer structure. Figures 1(a) and (b) illustrate the concentration of the Si isotopes versus depth of samples #1 and #2, respectively. The isotope profiles were measured with secondary ion mass spectrometry (SIMS). In order to prove the significance of isotopically modulated Si layers on the thermal conductivity, we also prepared by MBE 400 nm thick natural undoped Si layers on p-type Si wafer substrates with specific resistivities of $\sim 0.02\,\Omega\,\mathrm{cm}$ (sample #3) and $\sim 4\,\Omega\,\mathrm{cm}$ (sample #4). These samples, #3 and #4, with natural Si epilayers serve as reference

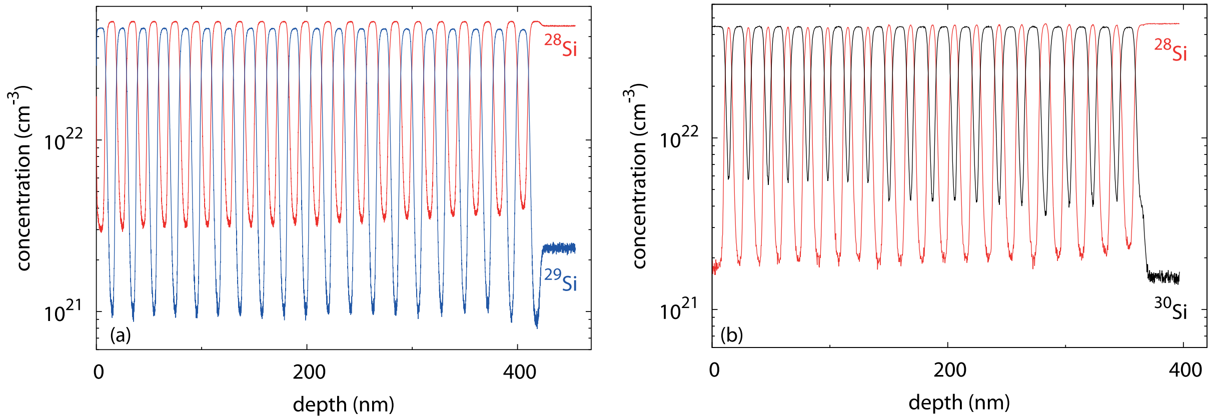

Figure 1. Concentration versus depth profiles of stable silicon isotopes in samples (a) #1 and (b) #2 measured with SIMS. Profiles of #1 and #2 represent isotope multilayer structures with 20 bilayers of (a) ^{29}Si/^{28}Si and (b) ^{30}Si/^{28}Si, respectively.

samples for the isotope samples #1 and #2, respectively. Moreover, we utilized a Si sample with a $\sim 90\,\mu$m thick enriched ^{28}Si layer (sample #5) doped with boron during CVD growth. The specific resistivity of the epilayer and the boron doped substrate is about 1 and 0.007 Ω cm, respectively.

Samples with lateral dimensions of $5 \times 5\,\text{mm}^2$ were cut from the wafers #1–#5, cleaned in organic solvents, etched in diluted hydrofluoric acid to remove the native oxide, and purged in deionized water. Immediately after cleaning, the epitaxial layers of the samples were covered first with a 2 nm thick chromium (Cr) layer and subsequently, i.e. without exposure to air, with a 28 nm thick gold (Au) layer by sputter deposition. The Cr layer between Si and Au enhances the adhesion of the Au layer and reduces the thermal resistance between the metal/Si interface [13, 14]. Since the thermal interface resistance strongly affects the heat transport from the metal layer to the Si, the isotope sample #1 (#2) and its reference #3 (#4) were processed simultaneously in pairs, i.e. cleaned and metal coated. In this way it is ensured that the thermal interface resistance between the metal layer and Si are similar for #1 and #3 (#2 and #4). Also sample #5 with the top isotopically enriched thick ^{28}Si layer and the polished backside of another piece of sample #5 were cleaned and coated simultaneously with a Au(28 nm)/Cr(2 nm) bilayer. The metal-coated natural Si back side of sample #5 serves as a reference sample (#6) for the top ^{28}Si epilayer of sample #5.

Gold layer thickness and film quality have been determined by x-ray reflectivity at the synchrotron beamline SCD at ANKA (Karlsruhe). The thermal conductivity of the epitaxial layers of samples #1–#6 is investigated by means of TRXS following pulsed laser excitation. This technique is described in the following section.

2.2. Heat transport measurements by time-resolved x-ray scattering

The thermal conductivity of the isotopically enriched epitaxial layers of samples #1, #2 and #5 is deduced from the cooling kinetics of the top metal layer in air after pulsed laser heating. This cooling behavior is affected by the thermal interface resistance and the thermal conductivity of the underlying material. The reference samples #3, #4 and #6, serve to determine the thermal interface resistance from the cooling behavior of the metal layer since the thermal conductivity

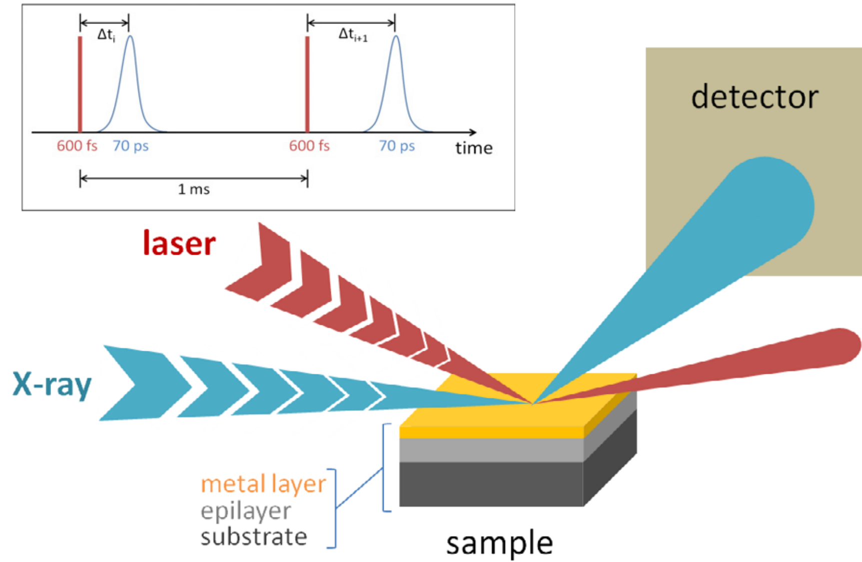

Figure 2. Schematic representation of the TRXS experiment conducted at the beam-line ID09B of the ESRF in Grenoble to investigate the thermal conductivity of an epitaxial isotopically modulated Si layer on a natural Si substrate. In this pump-and-probe experiment the laser pulse heats the top metal Au(28 nm)/Cr(2 nm) layer and, subsequently, the cooling of this metal layer is probed by x-ray pulses. The chronological sequence of the laser and x-ray pulses with their corresponding pulse width is indicated in the inset. Δt_i and Δt_{i+1} indicate the time delay between laser and x-ray pulses of two consecutive charge-coupled device (CCD) exposures. The time delay is varied up to 10 μs in order to record the cooling of the metal layer.

of natural Si is well known. This interface resistance is then assumed to describe the cooling behavior of the metal layer on top of the isotope sample that was metal deposited in the same sputter process.

The cooling of the metal layer after pulse-laser heating was followed by measuring the Au lattice constant with x-ray pulses as function of time. The utilized femtosecond laser system provides 600 fs pulses of 400 nm at a repetition rate of 1 kHz. The high thermal conductivity of the Au layer ($\sim$320 W m^{-1}K^{-1}) ensures that the heat supplied by the laser pulse spreads within about 60 ps in the metal film. X-ray pulses of 70 ps duration and 15 keV photon energy were reduced to the 1 kHz repetition rate of the laser by means of a rotating chopper. The laser pulses were synchronized to the x-rays to better than 5 ps. The two beams overlap spatially, i.e. the spot of the laser beam is about 500 μm in diameter while the width of the x-ray spot is about 100 μm. The pump-and-probe experiments were conducted at the beam-line ID09B of the European Synchrotron Radiation Facility (ESRF) in Grenoble [15, 16]. A silicon monochromator was used to select the 15 keV photon energy from the synchrotron beam. The time delay Δt between the two beams is varied up to 10 μs in order to record the cooling of the sample. The pump-and-probe experiment is schematically illustrated in figure 2. The incidence angle for the x-rays was the nominal Bragg angle for the Au (111) reflection at about 10°, while the laser struck the sample at 18° to the surface. The inset of figure 2 shows two consecutive laser pulses with the variable time delay Δt_i between laser and x-ray pulses and their corresponding pulse duration. In practice, an integration over the scattering response of about 2000 consecutive pulses at fixed delay was performed to increase the signal-to-noise ratio. The (111) Bragg peak of Au is

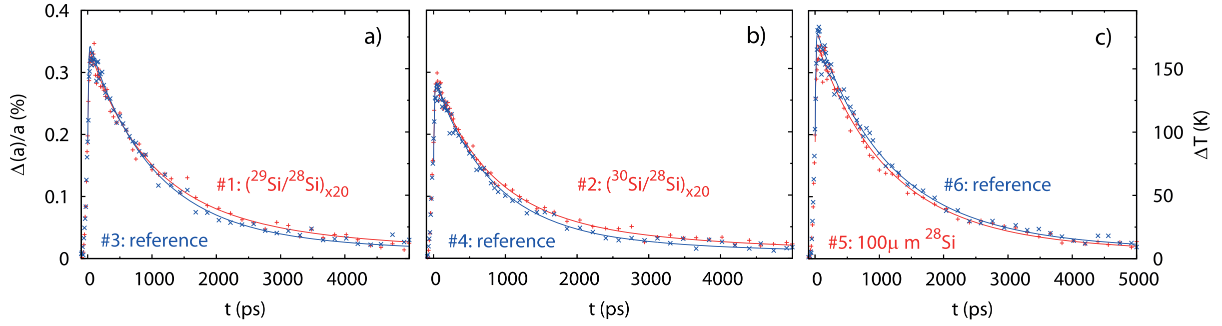

Figure 3. Time-resolved relative lattice expansion $\Delta a/a$ of a Au/Cr layer (symbols) deposited on top of different Si samples (#1–#6). The lattice expansion is measured by means of x-ray diffraction after heating the metal layer with a laser pulse. The left axis displays the relative lattice expansion $\Delta a/a$ and the right axis the corresponding temperature $\Delta T(t) = T - 300\,\mathrm{K}$. The solid lines represent best numerical fits to the experimental results (symbols). Panels (a) and (b) illustrate the expansion of the metal layer on top of the $(^{29}\mathrm{Si}/^{28}\mathrm{Si})_{20}$ (sample #1) and $^{30}\mathrm{Si}/^{28}\mathrm{Si})_{20}$ (sample #2) isotope multilayers in comparison to the reference samples #3 and #4, respectively. (c) Relative lattice expansion of the metal layer on top of a 90 μm thick isotopically enriched ^{28}Si layer (sample #5) in comparison to the reference sample #6.

recorded by a two-dimensional CCD detector. By measuring the angular position of the Bragg peak, it is possible to deduce the lattice expansion of the Au layer as function of time. The energy of the laser pulse that causes heating of the Au layer and thus the lattice expansion is adjusted in the linear response region, where a linear relationship between the pulse laser energy and the Au lattice expansion exists. The procedure is described in [13]. The temperature from the measured strain is estimated from the elastic uniaxial thermal expansion of a film fixed on a cold substrate.

Figures 3(a)–(c) illustrate the time-resolved relative lattice expansion of the Au layer on top of samples #1, #2 and #5 in comparison to the behavior of the Au layer on top of the corresponding natural Si reference samples #3, #4 and #6, respectively. The temperature of the metal layer is illustrated by the right y-axis. The time resolution of the experiment is mainly determined by the width of the x-ray pulse since the laser pulse is short compared to the x-ray pulse (see inset of figure 2). In order to determine the thermal conductivity of the epitaxial Si layer beneath the metal layer, the cooling of the metal layer as function of time is described by means of a heat transport model that is introduced in the following section.

2.3. Continuum theoretical simulation of heat transport

The structure considered for modeling the heat transport consists of a top metal layer deposited on an epitaxially grown Si layer. The epitaxial Si layer is grown on a natural Si substrate wafer and either represents the $(^{29}\mathrm{Si}/^{28}\mathrm{Si})_{20}$ multilayer of sample #1 or the $(^{30}\mathrm{Si}/^{28}\mathrm{Si})_{20}$ multilayer of sample #2 or the epitaxial natural Si layers of samples #3 and #4. In the case of the 90 μm thick ^{28}Si layer on a natural Si wafer (sample #5), a two-layer structure is considered because the epitaxial layer is sufficiently thick to distribute the heat homogeneously. Conceptually, the entire multilayer structure is considered as a homogeneous material with an effective heat conductivity. This effective value will serve to describe the potential of conductivity tailoring.

The metal coated backside of sample #5 representing the reference sample #6 is also described with a two-layer system consisting of the metal layer and the natural Si wafer substrate with a thickness ~600 μm. The heat injected by the laser pulse spreads from the metal layer over the epilayer into the wafer substrate. A constant thermal boundary conductance $\sigma_{\text{metal/Si}} = 1/R_{\text{K}}$, whose reciprocal value equals the Kapitza resistance R_{K}, is considered between the metal film and Si. The smaller size of the x-ray spot compared to the laser spot justifies to assume a one-dimensional heat transport from the metal layer into the Si sample.

The mathematical formulation of the heat transport problem is described by coupled partial differential equations with different heat diffusion coefficients for the metal film, epitaxial layer and the Si substrate in case of a three-layer system. For the two-layer system only two differential equations with appropriate heat diffusion coefficients are sufficient to describe the heat transport from the metal film into the isotopically enriched thick ^{28}Si layer or the natural Si substrate wafer. The differential equations are coupled via the boundary conditions established at the metal/Si interface. This heterointerface acts as a barrier for the heat transport. This is described by means of a Kapitza resistance R_{K}. Details about the differential equations and boundary conditions describing heat transport in a three-layer system as well as the relation between the heat diffusion coefficient and thermal conductivity λ_{epi} in the various epitaxial layers are given in [14]. A reduction to a two-layer system is straightforward and therefore not treated here. The system of differential equations is solved numerically considering the effective heat conductivity λ_{epi} in the isotopically modulated Si layers and the thermal boundary conductance $\sigma_{\text{metal/Si}}$ between metal/Si interface as free fitting parameters.

Previous experimental results and numerical calculations on heat transport in the three-layer system metal/Si-isotope-layer/Si-substrate reveal the importance of the thermal boundary conductance at the metal/Si heterointerface for an accurate determination of the heat conductivity λ of the isotopically modulated Si layer [14]. The higher the thermal boundary conductance the more sensitive is the cooling of the metal layer to the thermal conductivity of the subjacent isotopically controlled layer. This is demonstrated by TRXS experiments with Au- and Au/Cr-coated Si samples with and without an isotopically modulated layer [14]. For a Au-coated sample the thermal boundary conductance is about three times lower than that for a Au/Cr-coated sample. As a consequence the metal layer cooling of the Au-coated sample is less sensitive to the thermal conductivity of the isotope layer than in the case of the Au/Cr-coated sample. This demonstrates that the thermal boundary conductance $\sigma_{\text{metal/Si}}$ should be sufficiently high, i.e. $\sigma_{\text{metal/Si}} \approx 10^8\ \text{W m}^{-2}\ \text{K}^{-1}$, to be sensitive to the thermal conductivity of a layer with a thickness of only a few hundreds of nanometers. With respect to these results we deposited Au/Cr layers on Si samples to realize an acceptably high thermal boundary conductance. Moreover, Si samples of natural isotopic abundance that should be compared were coated in the same batch under equivalent conditions. These latter samples with known thermal conductivity serve as reference samples to determine $\sigma_{\text{metal/Si}}$ established in the sputter deposition process. This boundary conductance is then considered for Si samples with isotopically controlled layers that were metal deposited during the same sputter process. In this way only the thermal conductivity λ_{epi} of the isotope layer remains as the free-fitting parameter to describe the cooling of the metal layer after pulse laser heating. This strategy is schematically illustrated in figure 4. Note that the correlation between reference and isotope samples is applicable because the bonds established at the metal/Si interface only depend on the chemical nature of the elements involved. As all Si isotopes possess identical chemical properties, the bond

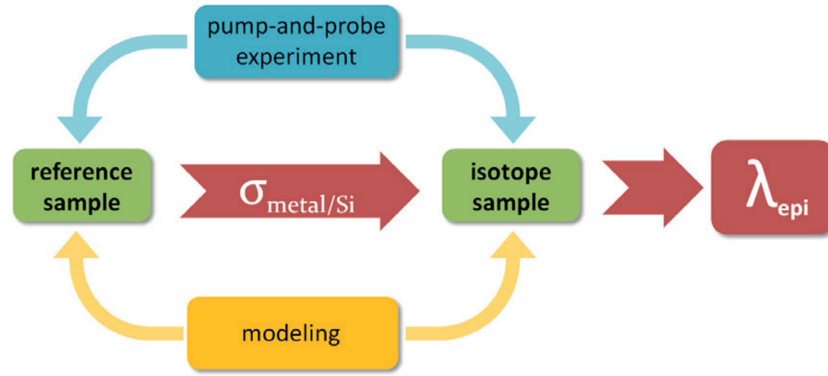

Figure 4. Schematic illustration of the procedure to determine the thermal conductivity λ_{epi} of an isotopically controlled epitaxial Si layer. Isotope and reference samples, respectively, with and without an isotopically controlled Si layer are investigated in the experiment. The experimental results are described by means of numerical simulations of the heat transport problem. Modeling the results of the reference sample provides the thermal boundary conductance $\sigma_{\mathrm{metal/Si}}$ at the metal/Si interface. This boundary conductance is then considered for modeling the cooling of the metal layer deposited on the isotope sample. Best fits to the experimental results yield the thermal conductivity λ_{epi} of the isotopically controlled epitaxial Si layer.

at the metal/Si interface remains unaffected when Si of natural abundance is replaced with isotopically enriched Si.

Figure 5 illustrates numerical simulations of heat transport in a three-layer system that consists of a metal layer, an epilayer, and a substrate as indicated in the inset. The laser pulse heats the metal layer and its cooling is recorded with time resolved measurements of the Au lattice expansion. The symbols shown in the right part of figure 5 demonstrate a typical relaxation of the Au lattice expansion as function of time obtained from the TRXS measurements of sample #1. The right y-axis illustrates the corresponding temperature ΔT of the metal layer deduced from the linear relation between the relative lattice expansion $\Delta a/a$ and ΔT. The solid line describes the best fit to the relaxation curve with λ_{epi} as a fit parameter. Beforehand the thermal boundary conductance $\sigma_{\mathrm{metal/Si}}$ was deduced from the relaxation curve of the reference sample. The left part of figure 5 gives more details on the heat transport simulation. Considering the three-layer system indicated by the inset, the heat injected by the laser pulse spreads out within the metal layer almost instantaneously, i.e. in about a few tens of picoseconds thanks to the high thermal conductivity of Au ($\lambda_{\mathrm{Au}} = 320\,\mathrm{W\,m^{-1}K^{-1}}$) and the boundary conductance at the metal/Si interface ($\sigma_{\mathrm{metal/Si}} \approx 10^{8}\,\mathrm{W\,m^{-2}\,K^{-1}}$). The value of $\sigma_{\mathrm{metal/Si}}$ was deduced from the simulation of the lattice expansion of the Au layer deposited on the reference sample. The left part of figure 5 illustrates temperature versus depth x profiles (see black solid lines) for various times t starting at 10 ps up to 5000 ps. The simulations clearly resolve the temperature drop at the metal/Si interface that decreases with increasing time according to the thermal boundary conductance and the heat diffusivities of the material on both sides of the interface [14]. The red solid line in the left part of figure 5 shows the average temperature of the metal layer as function of time. This profile is convolved with the resolution function of the x-ray pulse and compared to the experiment. This is indicated by the red solid line in the right part of figure 5. The simulations of the experimental results provide

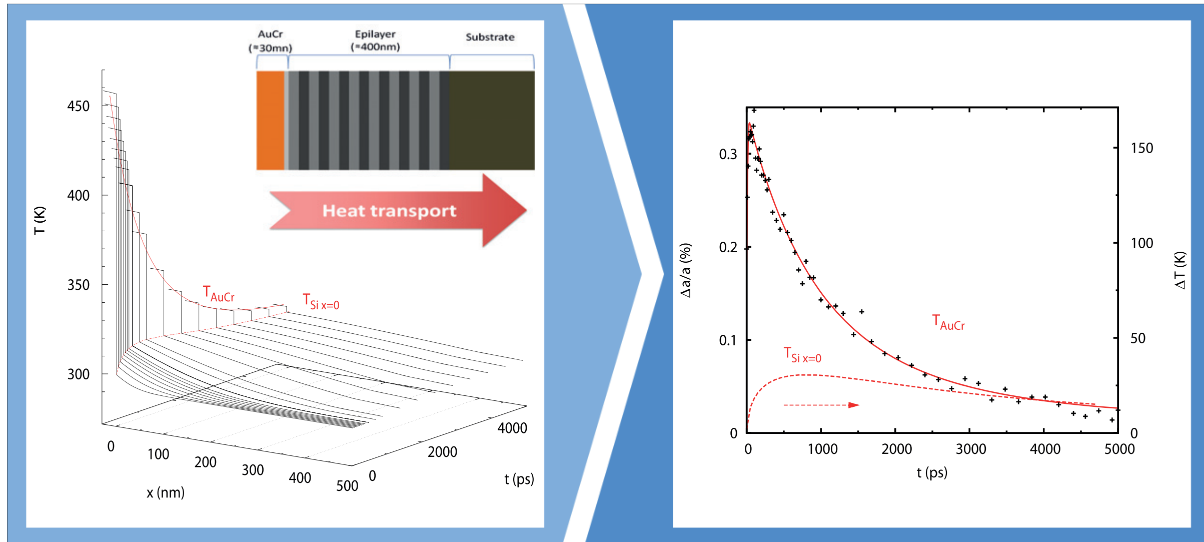

Figure 5. Illustration of the numerical calculation of heat transport in a three-layer system that consists of a metal layer, an epitaxial Si layer, and a Si substrate. The epitaxial layer represents an isotopically controlled Si layer or a Si layer of natural abundance. The three-layer structure is indicated by the inset on the left-hand side. The heat transport from the metal layer into the subjacent Si (see black solid lines on the left-hand side) is calculated for consecutive time steps until the temperature gradient at the metal/Si interface vanishes. The calculated average temperature of the Au layer and its cooling behavior indicated by the red solid line is compared on the right-hand side with the relative Au lattice expansion (+) measured after pulse laser heating of the metal layer. The lattice expansion is directly related to the temperature of the Au layer [13]. The temperature calculated for the Si side of the metal/Si interface is given by the red dashed line. The temperature at the Si side of the interface varies by about 25 K with time whereas the temperature of the Au layer changes by about 150 K. To a good approximation the thermal conductivity of Si is independent of temperature during the cooling process.

additional information about the temperature evolution at the Si side of the metal/Si interface. This temperature versus time profile is illustrated by the red dashed line both in the left and right part of figure 5. Whereas the temperature of the Au layer changes during cooling from about 450 K to room temperature, the temperature at the Si side of the metal/Si interface only varies by about 25 K. In this temperature range the thermal conductivity of Si changes at most by 10 $W\,m^{-1}K^{-1}$ considering the temperature dependence of the thermal conductivity in natural and isotopically enriched ^{28}Si reported in the literature [5–7]. Hence the variation in the thermal conductivity of Si is small during the pump-and-probe experiment. Therefore we can assume a temperature-independent thermal conductivity for the simulation of the heat transport in Si.

2.4. Results

The relative lattice expansion of Au layers after pulse laser heating was measured by TRXS for the metal deposited isotope samples #1, #2 and #5 and for the respective reference samples #3, #4 and #6. The best fits are shown by the solid lines in figure 3. Table 1 summarizes the thermal conductivity and thermal boundary conductance that were determined from the pump-and-probe experiments with the isotope and reference samples #1–#6.

Table 1. Thermal conductivity λ_{epi} of isotopically controlled silicon epitaxial layers (#1, #2, #5) determined from the pump-and-probe experiments described in this work. The respective reference samples (#3, #4 and #6) serve to define the thermal boundary conductance $\sigma_{metal/Si}$ at the metal/Si interface.

No.	Si material	λ_{epi} ($W\,m^{-1}K^{-1}$)	$\sigma_{metal/Si}$ ($W\,m^{-2}K^{-1}$)
#1	$(^{29}Si(10\,nm)/^{28}Si(10\,nm))_{20}/^{nat}Si$ wafer	60 ± 7	7.6×10^{7}[b]
#2	$(^{30}Si(10\,nm)/^{28}Si(10\,nm))_{20}/^{nat}Si$ wafer	58 ± 5	9.1×10^{7}[b]
#3	$^{nat}Si(400\,nm)/^{nat}Si$ wafer (reference for #1)	149[a]	$(7.6 \pm 0.2) \times 10^{7}$
#4	$^{nat}Si(400\,nm)/^{nat}Si$ wafer (reference for #2)	149[a]	$(9.1 \pm 0.3) \times 10^{7}$
#5	$^{28}Si(90\,\mu m)/^{nat}Si$ wafer	196 ± 19	6.6×10^{7}[b]
#6	^{nat}Si wafer (backside of #5, reference for #5)	149[a]	$(6.6 \pm 0.1) \times 10^{7}$

[a] Thermal conductivity of natural Si at 293 K [7].
[b] Set as equal to the value of the thermal boundary conductance of the respective reference sample.

The thermal conductivity of the 90 μm thick highly enriched ^{28}Si layer is with 196 $W\,m^{-1}K^{-1}$ higher than the thermal conductivity of Si with natural isotopic abundance. Within the experimental accuracy this supports the enhancement of about 10% reported in the literature for the thermal conductivity of pure ^{28}Si compared to natural Si [5–7]. In contrast, the thermal conductivities of the isotopically modulated $(^{29}Si/^{28}Si)_{20}$ (sample #1) and $(^{30}Si/^{28}Si)_{20}$ (sample #2) multilayers are clearly lower than that of natural Si (see table 1). The Kapitza resistance deduced from the analysis of the reference samples are equal within 20% for the different sputter deposition processes. The values given in table 1 indicate a similar reduction of the thermal conductivity for samples #1 and #2. Overall, the experimental results clearly demonstrate an impact of isotopic modulation on the thermal conductivity of Si and the question rises to which magnitude the thermal conductivity of Si can be altered by isotopic engineering. Since the preparation of Si isotope structures with different layer thicknesses, layer sequences, and layer numbers by means of MBE and their subsequent analysis with TRXS is by far too laborious and time consuming, we performed molecular dynamics (MD) calculations to determine the impact of various kinds of isotopic modulated Si layers on thermal conductivity.

3. Molecular dynamics simulation

3.1. Simulation setup

In order to theoretically study the effect of isotopic composition on the thermal conductivity of Si reverse non-equilibrium MD simulations were performed using the LAMMPS MD code [17]. In a MD simulation Newton's equations of motion $\vec{F} = m\,d^2\vec{r}/dt^2 = -\vec{\nabla}\Phi(\vec{r})$ are solved numerically and the positions and velocities of all atoms are determined. $\Phi(\vec{r})$ is a suitable interatomic potential. In our simulation we use the Stillinger–Weber potential for Si [18] with a timestep of 1 fs. As MD rely on classical mechanics, the simulations have to be performed at sufficiently high temperatures in order to avoid quantum effects [19]. In our case the average temperature of the sample is 400 K.

The simulation cell consists of $28 \times 10 \times 10$ unit cells of Si with a cell volume of 449 nm^3 (22 400 atoms) and a lattice constant of 5.431 Å. Periodic boundary conditions are enforced in

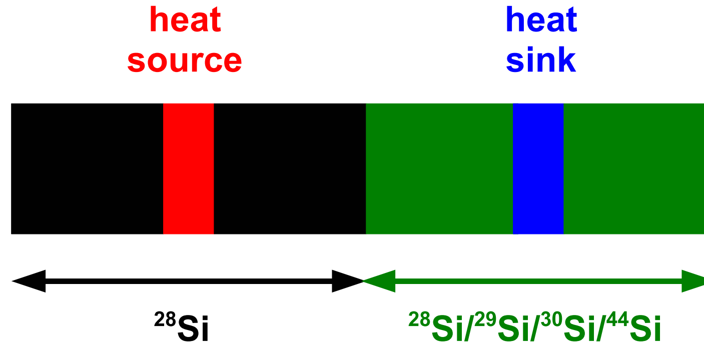

Figure 6. Sketch of the simulation cell and the isotopic modulation of the sample: The left half of the simulation cell consists of ^{28}Si and the right half of ^{28}Si, ^{29}Si, ^{30}Si or ^{44}Si. The heat source is located at one quarter of the length of the simulation cell and the heat sink at three quarters of the simulation cell.

the x-direction (cross-plane direction of the layered structure) and free boundary conditions in the y- and z-direction (in-plane direction of the layered structure). The initial velocities of the atoms are assigned by a random velocity distribution. A temperature gradient along the sample in the x-direction is established by adding an amount of non-translational kinetic energy (i.e. heat, aggregate momentum is conserved) to the atoms in the hot reservoir at every time step and subtracting the same amount of energy from the atoms in the cold reservoir. As periodic boundary conditions are enforced in the direction of the temperature gradient, the hot reservoir is located at one quarter of the sample length and the cold reservoir at three quarters of the sample length. This is illustrated in figure 6. The size of each reservoir is one unit cell in the x-direction and ten unit cells in the y- and z-direction, the added/subtracted amount of kinetic energy per time step $\mathrm{d}E/\mathrm{d}t$ is $20\,\mathrm{eV\,ps^{-1}}$. The temperature is determined locally for each atomic layer perpendicular to the x-direction. It is calculated from the kinetic energy assuming equipartition, $T = \langle mv^2\rangle/(3k_\mathrm{B})$, averaging over the atoms in the respective layer and the simulation time.

An effective thermal conductivity λ of the sample is calculated by means of Fourier's law [20] from the added amount of energy per time step $\mathrm{d}E/\mathrm{d}t$, the cross section area A of the sample, the resulting temperature difference ΔT, and the distance Δx between heat source and heat sink (see figure 7)

$$\lambda = -\frac{\frac{\mathrm{d}E}{\mathrm{d}t}\Delta x}{2\,A\,\Delta T}. \tag{1}$$

The factor two in equation (1) arises from the fact that half of the heat flows to the left and the other half to the right, because periodic boundary conditions are used (see figure 7) [21].

The effective thermal conductivity calculated from equation (1) is affected by the temperature anomalies at the heat source and sink, where the system, perturbed in every time step, is not able to relax into local equilibrium. These anomalies extend to about 2 nm on each side of the source and the sink. They could be neglected for much larger Δx than considered here. However, the boundary (or Kapitza) resistance R_K between the isotopic layers can be considered as unaffected by these anomalies already for our system size. For the interface between regions with atomic masses 28 and m (in atomic mass units) it is given by

$$R_\mathrm{K} = -\frac{2\Delta T - \Delta T(m=28) - \Delta T(m)}{\mathrm{d}E/\mathrm{d}t}A. \tag{2}$$

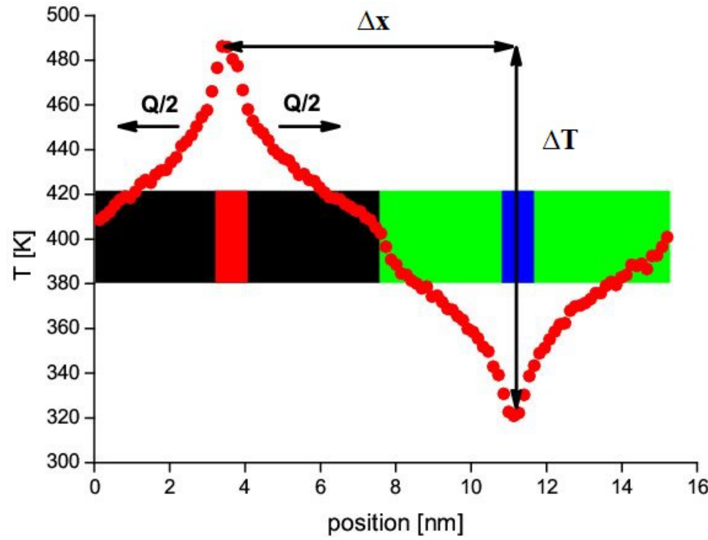

Figure 7. Temperature profile and isotopic modulation of a ^{28}Si(7.60 nm)/^{30}Si(7.60 nm) bilayer structure. The temperature gradient is determined from the temperature difference dT between heat source and heat sink divided by their distance dx. Due to periodic boundary conditions in the direction of the temperature gradient half of the heat $Q/2$ flows to the left side of the heat source and the other half of the heat flows to the right side of the heat source.

$\Delta T(m)$ is the temperature difference, if all atoms have the same mass m. It scales like $\sqrt{m}$ so that

$$\Delta T(m) = \sqrt{\frac{m}{28}} \Delta T(m = 28). \tag{3}$$

Equation (2) is derived by assuming that the total thermal resistance, $\frac{1}{\lambda}\frac{\Delta x}{A}$, is a sum of three terms. The first one, $\frac{1}{\lambda(m=28)}\frac{\Delta x/2}{A}$, is the thermal resistance of the left half of the system, where the atomic mass is 28. The second one, $\frac{1}{\lambda(m)}\frac{\Delta x/2}{A}$, is the thermal resistance of the right half. The interface contribution is described by the third term, R_{K}. Inserting equation (1) to relate $\lambda(m)$ to $\Delta T(m)$ leads to equation (2).

Two sets of Si samples are investigated in this work. In the first case the left half of the sample consists of ^{28}Si and the right half consists of ^{28}Si,^{29} Si, ^{30}Si or ^{44}Si. In this way the effect of mass difference on the thermal conductivity can be studied. In the second case, the impact of the superlattice period on thermal conductivity is examined. The sample is built up by a varying number of ^{28}Si/^{30}Si bilayers at fixed total sample length. The thermal conductivities calculated for the ^{28}Si/^{30}Si superlattice are compared with the thermal conductivities of $^{\mathrm{nat}}$Si, ^{28}Si and an ^{28}Si$_{0.5}$ ^{30}Si$_{0.5}$ alloy.

3.2. Results

3.2.1. Effect of mass difference. Figure 8 shows the steady state temperature profiles for four bilayer systems ^{28}Si/^{m}Si with $m = 28$, 29, 30 and 44. Note the different temperature scales of the four plots. The sharp temperature drop at the interface (at ≈ 7.6 nm) visible for $m \neq 28$ is due to the Kapitza resistance. It is evaluated according to equation (2) and plotted as a

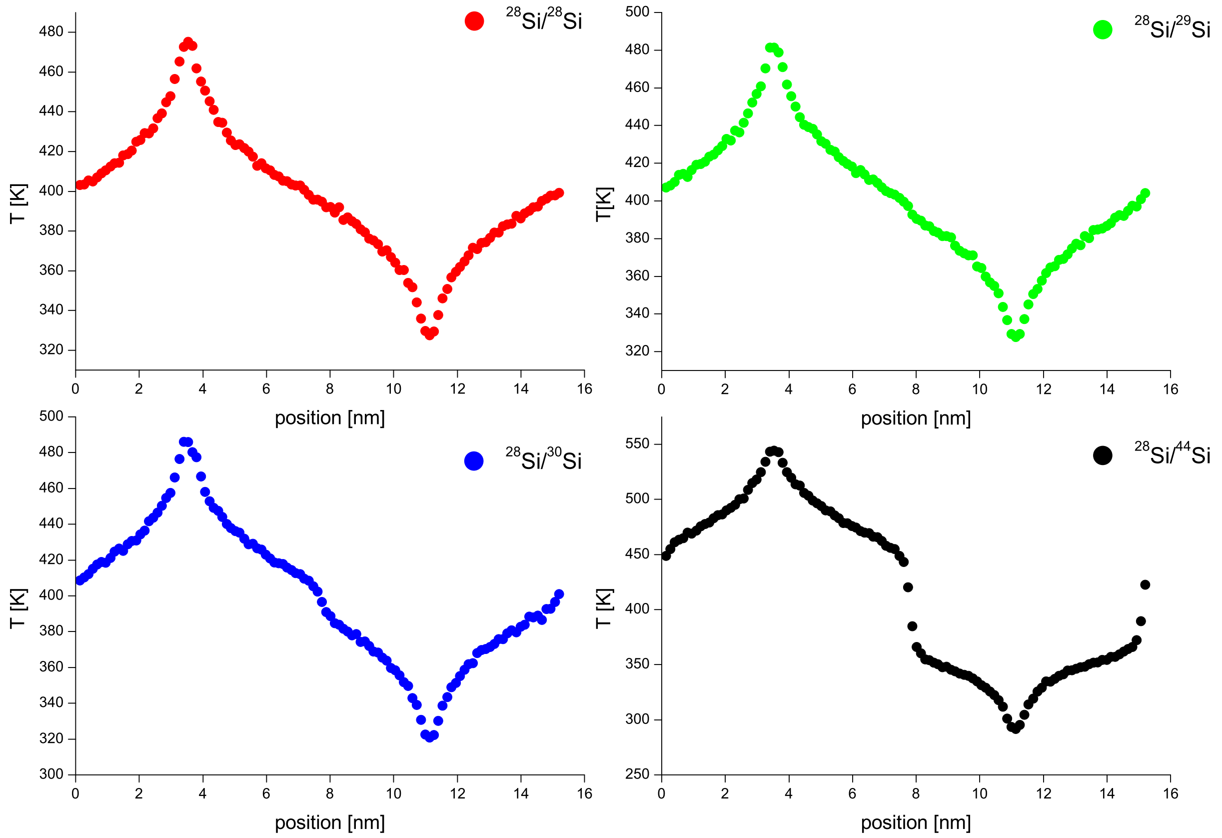

Figure 8. Temperature profiles for $^{28}Si/^{28}Si$ (top left), $^{28}Si/^{29}Si$ (top right), $^{28}Si/^{30}Si$ (bottom left) and $^{28}Si/^{44}Si$ (bottom right): the $^{28}Si/^{28}Si$ profile shows no step change in temperature at the interface as expected. In the three other cases the Kapitza resistance at the interface increases with increasing mass difference of the Si isotopes.

function of $\Delta m = m - 28$ in figure 9. A linear regression of $R_K = a\ \Delta m$ gives the value $a = 9.93 \times 10^{-11}\,\mathrm{K\,m^2\,W^{-1}u^{-1}}$.

The simulation result for the thermal conductivity of the pure ^{28}Si-system, $\lambda(28) = 2.79\,\mathrm{W\,m^{-1}\,K^{-1}}$, is far below the experimental value for bulk silicon. The reason is that the boundary conditions imply that we simulate a nanowire, not a bulk lattice. Here a reduction of thermal conductivity due to size confinement is indeed expected [22].

3.2.2. Effect of superlattice period. In order to investigate the effect of interfaces and layer thickness on the thermal conductivity of a $^{28}Si/^{30}Si$ superlattice the bilayer thickness (superlattice period) is altered at a fixed sample length. The longest period of about 15 nm is realized when one half of the simulation cell consists of ^{28}Si and the other half of ^{30}Si. The shortest period is 0.27 nm, i.e. the isotopic composition changes every monolayer. Figure 10 shows the thermal conductivity of a $^{28}Si/^{30}Si$ superlattice as function of the superlattice period. For comparison the thermal conductivities of ^{nat}Si, ^{28}Si and an $^{28}Si_{0.5}\ ^{30}Si_{0.5}$ alloy are also displayed.

Figure 10 reveals that a reduction in thermal conductivity of Si is possible by isotope doping. The higher thermal conductivity of ^{28}Si compared to ^{nat}Si is due to the absence of

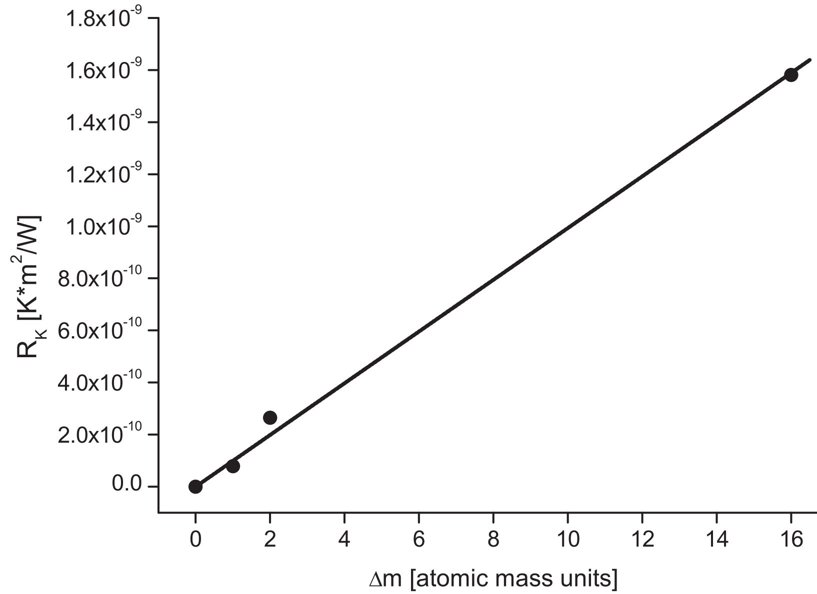

Figure 9. Kapitza resistance calculated for the isotope bilayer structures shown in figure 8 as function of the mass difference of the Si atoms on the right and left side of the interface. The solid line shows the result of the linear regression analysis.

phonon scattering by isotope defects. The $^{28}Si/^{30}Si$ superlattice and $^{28}Si_{0.5}$ $^{30}Si_{0.5}$ alloy have the same stoichiometric composition but a different spatial isotopic distribution. In the alloy the lattice sites are randomly occupied by ^{28}Si or ^{30}Si atoms, in the superlattice the ^{28}Si and ^{30}Si atoms are arranged in layers. This leads to different phonon scattering mechanisms: in the alloy the phonons are scattered by randomly distributed isotope defects and in the superlattice the phonons are scattered at the interfaces between ^{28}Si and ^{30}Si.

The thermal conductivity of the $^{28}Si/^{30}Si$ superlattice has a distinct minimum at a period length of 1.09 nm. This minimum appears at a length that is of the order of the effective phonon mean free path [23]. Yang *et al* [24] reported qualitatively the same effect of superlattice period on the thermal conductivity of $^{28}Si/^{29}Si$ and $^{28}Si/^{42}Si$ superlattices. The period length with minimum thermal conductivity is exactly the same. The behavior can be qualitatively understood in the following way. First a periodic arrangement with superlattice periods of only a few layers appears to be a homogeneous medium for long-wavelength phonons. Therefore contribution to phonon scattering will be low and the effect on the thermal conductivity is less pronounced. Once the layers increase in thickness, the thermal conductivity will drop. Increasing the superlattice period at fixed length of the simulation cell further will on the other hand, decrease the absolute number of scattering interfaces, consequently conductivity rises again.

The inset of figure 10 illustrates an increase of the thermal resistivity with increasing number of interfaces for superlattice periods equal to and greater than 1.09 nm. A linear increase is expected in case the thermal conductivity of the isotope superlattice is mainly given by serial connection of the interface resistances. However, our calculations clearly reveal a deviation from the linear dependence. The origin of this deviation is discussed in the next section.

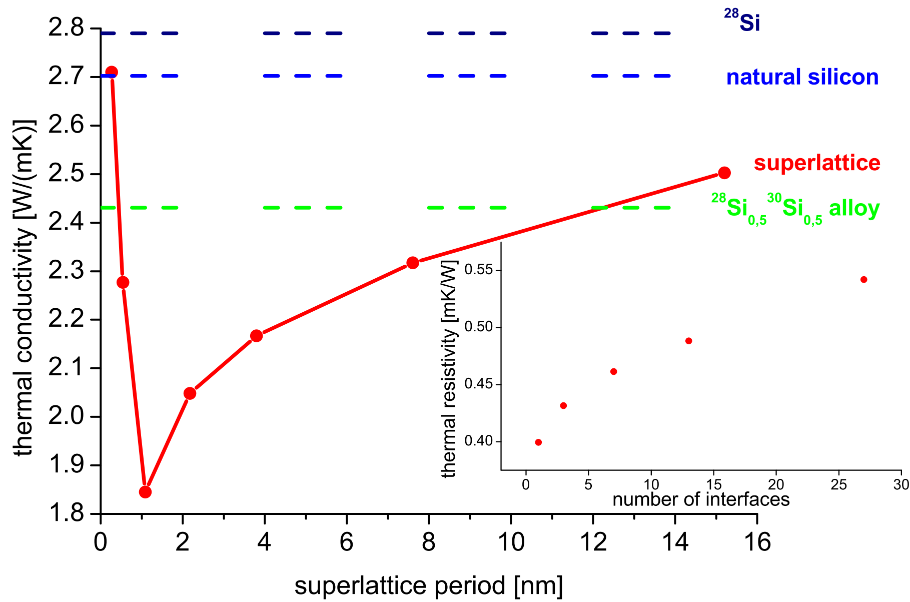

Figure 10. Thermal conductivity of an $^{28}Si/^{30}Si$ superlattice (red line and dots), ^{nat}Si (dashed blue line), ^{28}Si (dashed black line) and an $^{28}Si_{0.5}\,^{30}Si_{0.5}$ alloy (dashed green line). For the superlattice structure the thermal conductivity is plotted as a function of superlattice period, for the other three samples the lines are dashed as there is no isotopic periodicity within the samples. The inset demonstrates the thermal resistivity versus the number of interfaces. The calculations suggest an interrelation that clearly deviates from a linear dependence.

4. Discussion

Both experimental and theoretical results reveal a reduction in the thermal conductivity of silicon by isotopic modulation. The experiments indicate a factor of 2 to 3 lower thermal conductivity of the isotope multilayer structure compared with natural Si (see section 2.4 and [14]). MD simulations reveal a reduction of about 30% in thermal conductivity in comparison to the simulations of ^{nat}Si. Thus the simulations predict a much smaller reduction. This is related to the fact that MD calculations represent the thermal properties of a silicon nanowire. The main reduction of the thermal conductivity compared to natural bulk Si is due to the lateral confinement. An isotopic modulation gives only a modest further reduction.

As isotope heterostructures represent chemical and electronic homostructures, the reduction in thermal conductivity must be due to phonon scattering at the isotope interfaces. The scattering process at interfaces can be explained either with a diffuse or acoustic mismatch model. In the first case, the conductivity of a given multilayer is determined by the density of the interfaces, which scatter phonons incoherently. In the second case the coherent reflection of phonons will lead to complete stop bands for certain phonon wave vectors. A selective reflection or transmission of phonons has e.g. been reported for GaAs/AlGaAs superlattices by Narayanamurti *et al* [25]. The phonon scattering is similar to the reflection of electromagnetic waves at the interface between two optical media with different refractive indices [25]. Moreover, Spitzer *et al* [26] show clear evidence for optic phonon confinement in isotopically modulated germanium superlattices.

In the framework of the acoustic mismatch model, the phonons can be considered as waves whose mean free path is longer than the period length of the multilayer structure [27]. Within this limit the thermal conductivity of a multilayer structure will decrease with increasing superlattice period due to band-folding effects [27]. Band-folding reduces the phonon group velocities and thus the thermal conductivity [28, 29]. If the phonon mean free path is shorter than the period length, phonons can be treated as particles and diffuse scattering prevail. In this limit the thermal conductivity will increase with decreasing interface density. Accordingly, a minimum in thermal conductivity is expected as function of the superlattice period. This is supported by our MD simulation results shown in figure 10. A minimum in the thermal conductivity as function of the period length is also confirmed by MD calculations performed by Yang *et al* [24]. The minimum in thermal conductivity at a period length of 1.09 nm describes the crossover between a wave- and particle-type phonon transport [27], i.e. for period lengths below 1.09 nm the wave-like behavior and for period lengths above 1.09 nm the particle-like behavior of phonons prevails. In the first case the phonons are fully coherent and give rise to phonon bands specific for the superlattice structure. In the latter case, the phonons are fully incoherent and the thermal conductivity can be calculated by means of the Boltzmann transport equation assuming the diffused scattering at the interfaces [30]. This impact of coherent and incoherent phonons on heat transport in superlattices is treated theoretically and discussed in the literature in detail (see e.g. [31–33]). The inset in figure 10 suggests a nonlinear dependence of the thermal resistivity as function of the number of interfaces for period lengths larger than 1.09 nm. This dependence indicates that phonon coherence still affects the thermal conductivity at this length scale.

Although our MD calculations support a reduction in thermal conductivity by isotopic modulation, the absolute values obtained for the thermal conductivity of natural Si, isotopically enriched ^{28}Si, the $^{28}Si_{0.5}\,^{30}Si_{0.5}$ alloy and of the isotope superlattice deviate from the experimental results listed in table 1. The calculated thermal conductivity is much lower compared to the experiment. This is a consequence of the limited size of the simulation cell both in vertical and parallel directions of heat flow. In particular, the limited size affects the phonon mean free path, i.e. larger cells would yield larger phonon mean free path. Accordingly, phonons with long mean free path that significantly contribute to the thermal conductivity in bulk silicon are not considered by MD simulations [34]. Moreover, our calculations assume perfect interfaces that are hardly realized experimentally. The impact of interfacial mixing on phonon transport in silicon/germanium superlattices has been studied by Landry *et al* [30] with MD simulations. They observe that phonon coherence vanishes in the case of interface mixing and, consequently, an increase in thermal conductivity with increasing period length is suggested indicating incoherent phonon transport [30].

The measurements of the two samples #1 and #2 with different isotopic compositions ($^{28}Si/^{29}Si$) and ($^{28}Si/^{30}Si$) indicate similar thermal conductivities. The MD simulations reveal a further reduction of the thermal conductivity with increasing mass difference between the constituents of a superlattice in which the interfaces were assumed to be sharp (see figure 8). The comparison between experimental and theoretical results demonstrates the strong effect of the thermal interface resistance, which may cover the effect of the higher mass difference on the phonon transport in the experiment. This interface resistance is likely due to the interfacial mixing as discussed above. To understand more quantitatively the experimentally observed reduction in the thermal conductivity of silicon by isotopic modulation not only a mixing at the

isotope interfaces but also appropriate procedures to eliminate the size effect in MD simulations must be considered in the future MD simulations.

5. Conclusion

The experimental and theoretical results of this work lead to the conclusion that the acoustic mismatch model and the Fourier heat conduction theory based on bulk material properties do not explain in a satisfactory manner the effective thermal conductivity of isotopically modulated superlattice structures. The suggestion that the physical properties of the superlattice itself govern the thermal transport in such structures seems to be more convincing.

Thus far the argumentation includes a diffuse and acoustic mismatch model. In the first case, the conductivity of a given multilayer is determined by the density of the interfaces, which scatter phonons incoherently. In the latter case one may speculate about the influence of coherence on the phonon transport. In the optical picture [31, 35] of Bragg reflection of coherent phonons [32, 36] not only the presence of interfaces matters but also the periodic arrangement due to long mean free paths. A multilayer represents a Bragg grating that can efficiently block complete phonon bands. On the other hand a periodic lattice might not be the optimal structure, as compared to tailored aperiodic or chirped layer stacks. Such tailored structures will be investigated in future by combining predictions from MD simulations with experimental tests. These studies will help to identify more quantitatively the factors that determine the thermal conductivity in isotopically modulated silicon.

Tailored silicon structures may find applications as thermoelectric power generators or refrigerators in high temperature applications or highly integrated miniaturized devices. The ultimate power factor needs to be proven.

Acknowledgments

Provision of beamtime at the facilities ANKA and ESRF is gratefully acknowledged. We wish to thank for the excellent support by M Khakulin, M Wulff and G Buth. This work was funded by the Deutsche Forschungsgemeinschaft via the priority program SPP1386 ‘Nanostructured Thermoelectric Materials: Theory, Model Systems and Controlled Synthesis’ (BR 1520/13-1 and BR 1520/15-1) and individual grants for AP and within the Heisenberg program for HB (BR 1520/10-2). The isotopically enriched Si was developed by the Initiatives for Proliferation Prevention Program of the Office of Nonproliferation Research and Engineering (NN-20) of the U.S. Department of Energy under contract DE-AC03-76SF00098. Stimulating discussions with G Bastian, A Vogelsang and C Heiliger are acknowledged.

References

[1] Kishi M, Nemoto H, Hamao T, Yamamoto M, Sudou S, Mandai M and Yamamoto S 1999 *Proc. 18th Int. Conf. on Thermoelectrics* p 301

[2] Lay-Ekuakille A, Vendramin G, Trotta A and Mazzotta G 2009 *Proc. 2009 IEEE Int. Workshop on Medical Measurements and Applications* p 1

[3] Snyder G J and Toberer E S 2008 *Nature Mater.* **7** 105

[4] Bhandari C 1994 *CRC Handbook of Thermoelectrics* ed D M Rowe (Boca Raton, FL: CRC)

[5] Ruf T, Henn R W, Asen-Palmer M, Gmelin E, Cardona M, Pohl H-J, Devyatych G G and Sennikov P G 2000 *Solid State Commun.* **115** 243–7

[6] Ruf T, Henn R W, Asen-Palmer M, Gmelin E, Cardona M, Pohl H-J, Devyatych G G and Sennikov P G 2003 *Solid State Comm.* **127** 257

[7] Kremer R K, Graf K, Cardona M, Devyatych G G, Gusev A V, Gibin A M, Inyushkin A V, Taldenkov A N and Pohl H-J 2004 *Solid State Commun.* **131** 499–503

[8] Zollner S, Cardona M and Gopalan S 1992 *Phys. Rev.* B **45** 3376
Zollner S, Cardona M and Gopalan S 1992 *Phys. Rev.* B **46** 7337

[9] Karaiskaj D, Thewalt M L W, Ruf T, Cardona M and Konuma M 2002 *Solid State Commun.* **123** 87

[10] Thewalt M L W 2005 *Solid State Commun.* **133** 715

[11] Geballe T H and Hull G W 1955 *Phys. Rev.* **98** 940

[12] Ryu H J, Aksamija Z, Paskiewicz D M, Scott S A, Lagally M G, Knezevic I and Eriksson M A 2010 *Phys. Rev. Lett.* **105** 256601

[13] Issenmann D, Wehmeier N, Eon S, Bracht H, Buth G, Ibrahimkutty S and Plech A 2013 *Thin Solid Films* **541** 28–31

[14] Bracht H, Wehmeier N, Eon A, Plech A, Issenmann D, Lundsgaard Hansen J, Nylandsted Larsen A, Haller E E and Ager I I I J W 2012 *Appl. Phys. Lett.* **101** 064103

[15] Plech A, Grésillon S, von Plessen G, Scheidt K and Naylor G 2004 *Chem. Phys.* **299** 183

[16] Cammarata M *et al* 2009 *Rev. Sci. Instrum.* **80** 15101

[17] Plimpton S 1995 *J. Comput. Phys.* **117** 1–19

[18] Stillinger F H and Weber T A 1985 *Phys. Rev.* B **31** 5262

[19] Turney J E, McGaughey A J H and Amon C H 2009 *Phys. Rev.* B **79** 224305

[20] Schelling P K, Phillpot S R and Keblinski P 2002 *Phys. Rev.* B **65** 144306

[21] Jund P and Jullien R 1999 *Phys. Rev.* B **59** 13707

[22] Grauby S, Puyoo E, Rampnoux J-M, Rouvière E and Dilhaire S 2013 *J. Phys. Chem.* C **117** 9025

[23] Chen Y, Li D, Lukes J, Ni Z and Chen M 2005 *Phys. Rev.* B **72** 174302

[24] Yang N, Zhang G and Li B 2008 *Nano Lett.* **8** 276

[25] Narayanamurti V, Störmer H L, Chin M A, Gossard A C and Wiegmann W 1979 *Phys. Rev. Lett.* **43** 2012–6

[26] Spitzer J, Ruf T and Cardona M 1994 *Phys. Rev. Lett.* **72** 1565

[27] Simkin M V and Mahan G D 2000 *Phys. Rev. Lett.* **84** 927

[28] Ren S Y and Dow J D 1982 *Phys. Rev.* B **25** 3750

[29] Tamura S and Tanaka Y 1999 *Phys. Rev.* B **60** 2627

[30] Landry E S and McGaughey A J H 2009 *Phys. Rev.* B **79** 075316

[31] Ezzahri Y, Grauby S, Rampnoux J M, Michel H, Pernot G, Claeys W, Dilhaire S, Rossignol C, Zeng G and Shakouri A 2007 *Phys. Rev.* B **75** 195309

[32] Chen G 1998 *Phys. Rev.* B **57** 14958

[33] Yang B and Chen G 2003 *Phys. Rev.* B **67** 195311

[34] Sellan D P, Landry E S, Turney J E, McGaughey A J H and Amon C H 2010 *Phys. Rev.* B **81** 214305

[35] Bastian G, Vogelsang A and Schiffmann C 2010 *J. Electron. Mater.* **39** 9

[36] Sondhauss P, Larsson J, Harbst M, Naylor G A, Plech A, Scheidt K, Synnergren O, Wulff M and Wark J S 2005 *Phys. Rev. Lett.* **94** 125509